Direct observation of tensile-strain-induced nanoscale magnetic hardening

Deli Kong[1,2], András Kovács[1]*, Michalis Charilaou[3], Fengshan Zheng[1,4], Lihua Wang[5], Xiaodong Han[5]* and Rafal E. Dunin-Borkowski[1]

[1] Ernst Ruska-Centre for Microscopy and Spectroscopy with Electrons and Peter Grünberg Institute, Forschungszentrum Jülich, Jülich, 52428, Germany.

[2] School of Physics and Optoelectronics, Faculty of Science, Beijing University of Technology, Beijing, 100124, China.

[3] Department of Physics, University of Louisiana at Lafayette, Lafayette, Louisiana 70504, United States.

[4] Spin-X Institute, School of Physics and Optoelectronics, South China University of Technology, Guangzhou, China.

[5] Institute of Microstructure and Properties of Advanced Materials, Beijing University of Technology, Beijing 100124, China.

*Corresponding authors Email: a.kovacs@fz-juelich.de, xdhan@bjut.edu.cn

Abstract: Magnetoelasticity is the bond between magnetism and mechanics, but the intricate mechanisms *via* which magnetic states change due to mechanical strain remain poorly understood. Here, we provide direct nanoscale observations of how tensile strain modifies the magnetic field in a ferromagnetic Ni thin plate using *in situ* Lorentz transmission electron microscopy and off-axis electron holography. We observe the formation and dissociation of strain-induced periodic 180º magnetic domain walls perpendicular to the strain axis. The magnetization transformation exhibits stress-determined directional sensitivity and is reversible and tunable through the size of the nanostructure. Our results provide direct evidence for expressive and deterministic magnetic hardening in ferromagnetic nanostructures, while our experimental approach allows quantifiable local measurements of strain-induced changes in the magnetic states of nanomaterials.

Studies of the link between structure and magnetism in materials have a long history, dating back to the 19th century, when J. Joule and E. Villari discovered magnetostriction and magnetoelasticity. Since then, stress and stress annealing have found applications in the sensing, control and enhancement of magnetic properties in a wide range of materials and devices[1], ranging from magnetic random-access memory[2-4] to energy harvesting[5-7] and biomedicine[8,9].

Strain and magnetostriction are two key parameters that influence the formation of anomalous magnetic properties in thin films, which that lead to rotatable anisotropy and the formation of high-density stripe domains[10-13]. The ability to control the residual stress that gives rise to stress impedance effects has found applications in highly sensitive magnetic field sensors[14]. However, strain-induced effects on magnetism *on the nanoscale* remain poorly understood, primarily due to the experimental challenge of measuring and quantifying magnetic fields in nanomaterials, while at the same time allowing local control over strain. Such effects can be studied by observing the rearrangement of magnetic domains in the presence of strain, while making measurements of magnetic domain wall width, which is highly sensitive to fundamental and induced magnetic properties. However, commonly-used magnetic imaging techniques are limited to observing surface magnetic states[5,15] or are unable to provide quantitative magnetic information. Magnetic imaging methods based on transmission electron microscopy (TEM) such as Fresnel defocus imaging, differential phase contrast (DPC) imaging[16] and electron holography (EH)[17-19] can, in principle, be used to study magnetic domain walls quantitatively, as well as their rearrangements in the presence of external stimuli. Lorentz TEM imaging has been used to observe the effect of elastic stress on magnetic solitons in chiral magnets upon cooling[20,21]. In addition to magnetic domain wall imaging, high-spatial-resolution magnetic imaging of the interplay between electromagnetic fields and strain in ferromagnetic nanostructures and judicious control of this phenomenon also promises to provide routes towards the functional sensing of strain fields in materials.

Here, we present high-resolution measurements of magnetoelastic coupling between tensile strain and magnetization in a single-crystalline Ni nanostructure recorded using *in situ* TEM and off-axis EH. We directly observe the modification of internal anisotropy fields *via* the formation of highly structured magnetic domain walls. We compare our results with micromagnetic simulations to quantify the strain-induced anisotropy field and use them to explain how strain can be used to control the susceptibility of thin ferromagnetic metals. As Ni has negative magnetostriction[22, 23], strain induces orthogonal rotation of the magnetization. By using a bimetallic deformation device[24] and off-axis EH, we visualize magnetic texture changes quantitatively in real space during tensile straining of a single crystalline Ni sample. In order to assess the reproducibility of the results, we perform multiple tensile straining and release cycles up to the plastic deformation régime in magnetic-field-free conditions. Details of sample fabrication, the geometry of the experiment and magnetic imaging are given in the Methods section.

Results

***In situ* straining and magnetic imaging.** Direct observations of strain-induced effects on the magnetic domain state of the Ni sample were carried out by recording Fresnel defocus images and off-axis electron holograms during the application of tensile strain. The dynamical displacement of magnetic domain walls was observed as the strain was increased to 0.2 % and then decreased to 0 %. Movie s1 in the Supplementary Information shows the observed domain wall dynamics as a function of strain. The specifics of the magnetic transition were studied by visualizing the projected in-plane magnetic field inside and outside the specimen using EH.

Maps of projected in-plane magnetic induction are shown in Fig. 1 during a 2nd tensile cycle from 0 to 0.2 % strain. Fig. 1a shows a bright-field (BF) TEM image of the Ni sample before the 2nd tensile cycle. The sample is single crystalline and shows no sign of structural defects, with the crystallographic [110] orientation nearly horizontal and parallel to the strain direction, which is marked with a double-headed red arrow. (The first tensile cycle that was used to determine the starting point for magnetic domain rearrangement is shown in Fig. s5).

Figure 1b reveals directly, in the form of magnetic field lines and colors, that the unstrained Ni sample comprises a magnetic domain structure of low angle (<90º) magnetic domain walls. The magnetic stray field is also recorded in the form of contours around the sample. Strikingly, when the tensile strain is increased to 0.05%, the magnetic field lines turn to lie perpendicular to the direction of tensile strain. Figures 1c-e show the evolution of the magnetic domain structure as the tensile strain is gradually increased to 0.2 %. The low angle magnetic domain walls transform to 180º domain walls, which are perpendicular to the strain axis. The 180° domain walls form a lattice. We also observe that the stray field intensifies outside the sample (Fig. 1b-e) despite the formation of flux closure domains as the system attempts to minimize the magnetostatic energy (marked with red arrows in Fig. 1c). The strength of the magnetic stray field outside the sample increases with strain as a result of increasing magnetostatic energy due to alignment in the domains and decreasing domain wall thickness, as discussed below.

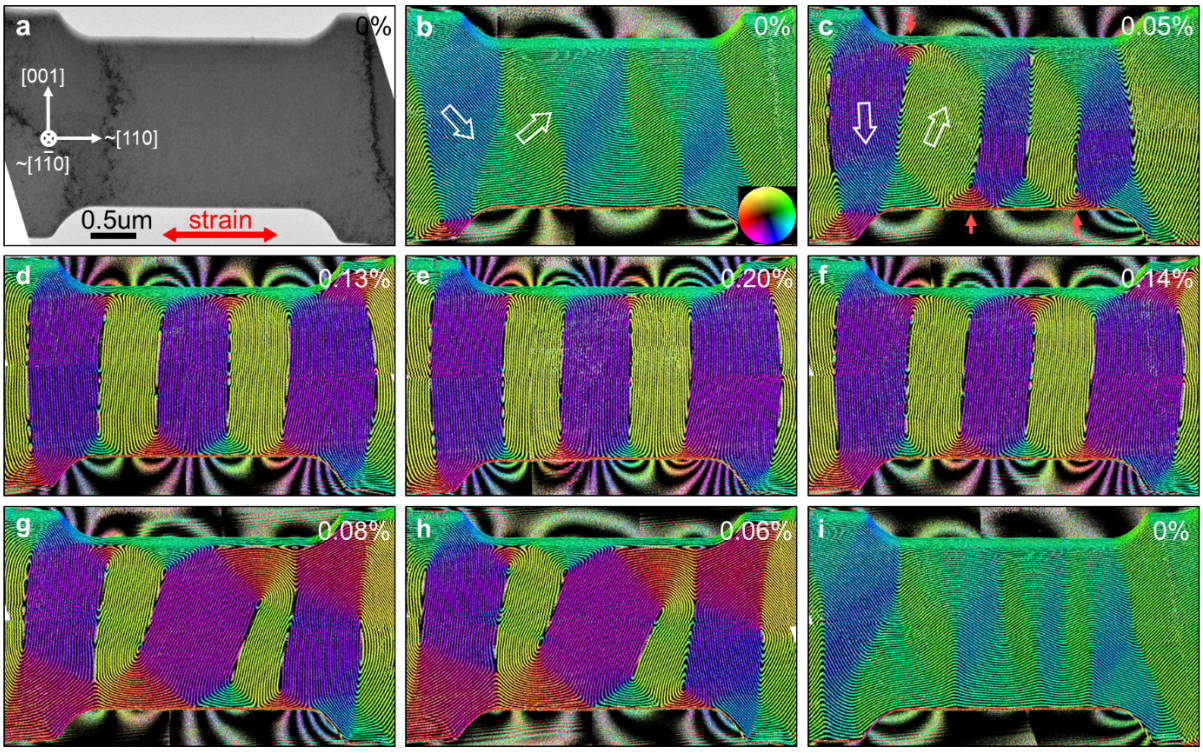

Fig. 1. Direct measurement of magnetostriction in a Ni nanostructure. **a** BF TEM image of a single crystalline Ni nanostructure recorded before a 2nd tensile cycle. The white arrows mark the crystallographic orientation of the sample. Strain was applied in the horizontal direction (marked by a double-headed red arrow) at the levels indicated in the upper right corner of each image. The error is estimated to be ±0.04%. **b - i** Real space magnetic induction maps recorded during a straining and release cycle using off-axis EH. The direction of the projected in-plane magnetic field is visualized both according to the color wheel shown in **b** and using hollow white arrows. The contour spacing is $2\pi/3$ radians. The small red arrows in **c** mark the positions of magnetic flux closure domains.

The magnetic induction maps in Fig. 1 reveal the formation of periodic magnetic domains, which are separated by 180º magnetic domain walls perpendicular to the strain axis. In this experiment, the strain was released before the formation of any observable plastic deformation (*i.e.*, before the formation of visible defects). On decreasing the strain to 0% (Figs 1f to 1i), the magnetic domains transform back to a configuration that is comparable to the pristine condition, suggesting a reversible magnetostrictive process up to a strain of 0.2 % (see also Movie s1). We observed similar strain-induced magnetic response in Ni samples with different crystallographic orientations, as shown in supplementary Fig. s7.

Magnetic domain wall structure. In order to *quantify* the relationship between strain and magnetic texture, we measured the evolution of magnetic *domain wall width* with strain from the derivative of the phase shift measured using EH[25,26] across two domains with a field rotation of 180º (Fig. s3). The domain wall width was measured as a function of strain based on fits to the data, as shown using blue dots in Fig. 2a.

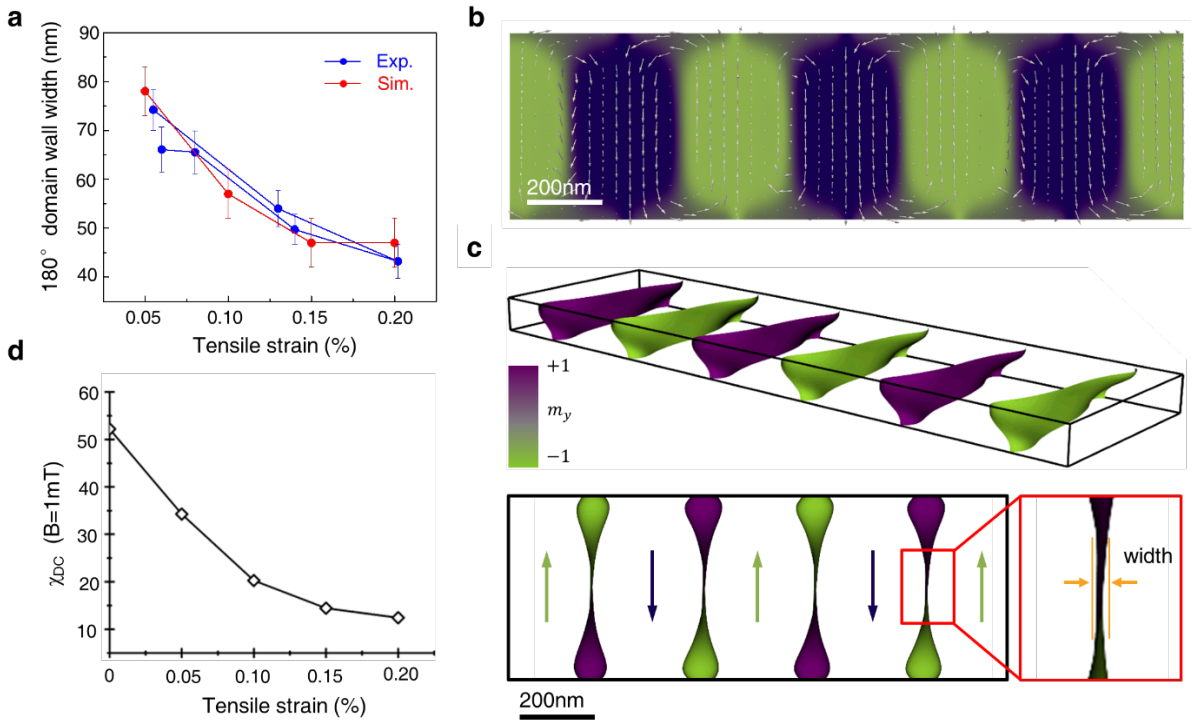

Fig. 2. Evolution of magnetic domain wall width with strain in a Ni nanostructure. **a** 180° magnetic domain wall width measured as a function of tensile strain during the 2nd tensile cycle using off-axis EH compared with micromagnetic simulations. **b** Representative micromagnetic simulation of Ni in the presence of 0.2 % strain. **C** Magnetic domain wall iso-surfaces showing the three-dimensional shapes of the walls, which are twisted from edge to edge. With increasing strain, both twisting of the domain walls and the average magnetic domain wall thickness decrease. **D** DC magnetic susceptibility of the Ni nanostructure plotted as a function of tensile strain.

Strikingly, a significant decrease in magnetic domain wall width from 75 to 43 nm is observed when the tensile strain is increased from 0.05 to 0.2 %. The magnetic domain wall width was determined for both straining and release cycles, confirming that the changes are reversible. The dramatic decrease in measured magnetic domain wall width δ with strain (by a factor of ~2) suggests that the ratio between exchange stiffness and effective anisotropy decreases by a factor of ~4 given that $\delta = \pi\sqrt{A/K}$, where A is the exchange stiffness and K is the magnetic anisotropy. This result, in turn, suggests that the strain-induced anisotropy is 3 times larger than the shape anisotropy of the thin film. However, considering that the shape anisotropy is on the order of 10^5 J/m^3, the latter interpretation is highly unlikely.

Instead, the apparent domain wall sharpening can be explained by considering the variation of the domain wall shape within the sample, considering that "*The domain wall is a three-dimensional object. The results obtained on thin films might be misleading*", as stated by

Arrott[27]. This statement inspired a deeper study of the effect of strain on the magnetic state and an inspection of the magnetization arrangement of the 180º domain walls in three dimensions (3D) using detailed micromagnetic simulations. The strain-induced micromagnetic state was simulated using a model that was based on the structure and dimensions of the Ni sample derived from imaging data and from a measurement of the sample thickness using electron energy-loss spectroscopy (Fig. s2). In the model, the sample had dimensions (length × width × thickness) of 2000 × 500 × 100 nm^3, while each simulation cell had a volume of 2 × 2 × 2 nm^3. The total energy density included contributions from ferromagnetic exchange, cubic magnetocrystalline anisotropy and long-range dipole-dipole interactions (magnetostatics). Stress in the Ni film was incorporated in the simulations in the form of easy-plane anisotropy[28] perpendicular to the strain direction, *i.e.*, normal to the [110] crystallographic axis. Strain-induced anisotropy (K_s) can be written in the form

$$K_s = -\frac{3}{2}\frac{Y}{(1+\mu)}\lambda\varepsilon$$

where Y = 200 GPa is the Young's modulus, μ = 0.3 is the Poisson ratio, $\lambda_{110} = -31\times10^{-6}$ is the magnetostriction coefficient and ε is the strain. The calculated value of strain-induced anisotropy is predicted to be between ~4 and ~15 kJ/m^3 for strains of between 0.05 and 0.2 %, respectively. The corresponding changes in magnetic state are summarized in Fig. s4.

As stated above, these values of strain-induced anisotropy *do not* explain the reduction in magnetic domain wall width that are observed experimentally in Fig. 2a. However, the *simulated* magnetic domain wall structures capture the intricate details of the underlying strain-induced effects (Figs 2b and 2c). Fig. 2b shows the magnetic state in the presence of 0.20 % strain in plan-view. Even though the magnetic field directions align perpendicular to the strain direction in the same way as in the experimental results shown in Fig. 1, analysis of the 3D magnetization distribution in the simulations reveals that the iso-surface of the wall is *twisted* from edge to edge, even at a relatively low level of strain, thereby appearing wider in *projected* images than its true thickness. With increasing strain, twisting of the domain walls scales down, leading to edge-on-views of the domain wall in the [1-10] direction, as shown in Fig. 2c. The *projected* domain wall width measurements from the simulation results are plotted in Fig. 2a and are in excellent agreement with the experimental observations.

The qualitative and quantitative agreement between the experiments and simulations allows the simulations to be used to predict further properties of strained Ni nanostructures and their response to external magnetic fields that cannot be measured directly. Fig. 2d shows micromagnetic simulations of DC magnetic susceptibility, which is plotted as a function of strain predicted by simulating hysteresis curves of the same Ni sample in the presence of different values of strain. The strong decrease in susceptibility with tensile strain indicates substantial magnetic hardening of the Ni nanostructures. The fact that the response of thin ferromagnetic films to external fields can be tuned by mechanical strain is of great importance for a wide range of applications, in part those that involve *sensing of strain*.

Discussion

Plastic deformation. In order to obtain insight into how the magnetic state evolves in the non-elastic regime, additional experiments were performed, where the sample was strained until evidence of plastic deformation was observed, as shown in Fig. 3. As the strain was increased gradually, the magnetization again rotated in a direction perpendicular to the strain (Fig. 3a,b), similar to the behavior shown in Fig. 1. However, once the elastic limit was exceeded at a strain of ~0.35 % (Fig. 3c), stacking fault formation was identified, as confirmed by the BF TEM image shown as an inset to Fig. 3c.

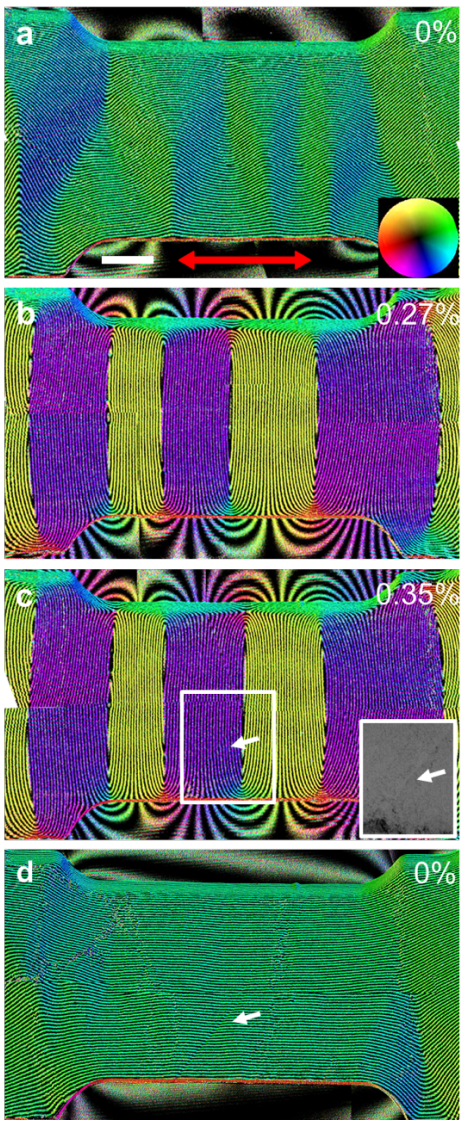

Fig. 3. Influence of plastic deformation on magnetic texture. a-c Magnetic induction maps of the Ni nanostructure recorded before and after applying tensile strains of **b** 0.27 % and **c** 0.35 %, at which stacking fault formation was observed. The strain direction is marked by a double-headed red arrow. The inset in **c** is a BF TEM image corresponding to the white rectangular area. **d** Magnetic structure after the stress was released. White arrows in **c, d** mark a stacking fault. In each image, the direction of the projected in-plane magnetic field is visualized according to the color wheel shown in **a**. The scale bar is 500 nm.

The stacking faults had no observable effect on the magnetic structure during the release process until the strain had been removed completely, as shown in Fig. 3d. Interestingly, at 0 % strain the magnetic domain structure was different after plastic deformation from that observed for the elastic cycles (Figs 1b and 3a), with a nearly uniform in-plane magnetic field and the 90º domain walls eliminated. Despite the observed lack of reversibility of the magnetic state, when the strain was *re-applied* the magnetic state returned to the same configuration as before, with domain walls perpendicular to the strain direction. These observations reveal the robustness of the magnetoelastic effect even when inverse magnetostriction is followed beyond the elastic limit in a nanostructure. Another straining cycle was conducted on the lamella following stacking fault formation, as shown in movie s2. The dynamic behavior of the magnetic domain walls under straining and release was observed to be similar to that for the plastic case.

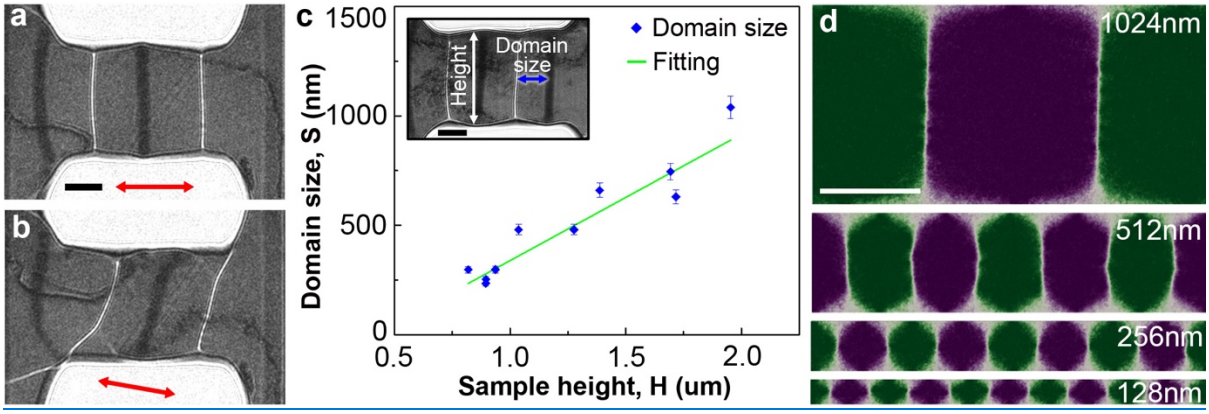

Fig. 4. Characteristic magnetic property changes in a strained Ni nanostructure. **a**, **b** Fresnel defocus images of the Ni nanostructure, demonstrating directional control of magnetization by stress. The double-headed arrow marks the applied strain direction. **c** Effect of the height of the Ni nanostructure on magnetic domain size at fixed tensile strain (0.20 ± 0.05 %). The linear fit is S = 0.58H-0.24, with an adjusted R-squared value of 0.85. **d** Micromagnetic simulations of Ni nanostructures of varying height at 0.20 % strain, showing changes in magnetic domain density. The scale bar is 500 nm.

We tested the directional dependence of magnetization control *via* stress by changing the strain direction relative to the film geometry. When the strain was parallel to the long horizontal side of the film, as in the original experiments, the directions of the in-plane magnetization and the magnetic domain walls were perpendicular to the strain direction, as shown in the form of a Fresnel defocus image in Fig. 4a. Directional control was achieved by manipulating the strength of the connection between the hook and the bimetallic deformation device. When the strain direction was changed by 9°, the magnetization direction also changed, as shown in

Fig. 4b and movie s3, reconfirming the possibility of directional control of magnetization by strain. Furthermore, both our experimental observations and corresponding micromagnetic simulations revealed a correlation between the height of the Ni nanostructures and the sizes of the magnetic domains under tensile conditions. Fig. 4c shows the dependence of magnetic domain size (defined to be the distance between two 180° domain walls) on sample height. (See also Fig. s9). The observed dependence is linear as a result of a balance between magnetostatic energy (which scales with volume) and magnetic domain wall energy (which scales with domain wall area).

In summary, we have combined experimental observations with micromagnetic simulations of magnetoelastic coupling between tensile strain and magnetic state to show that the application of strain to a single-crystalline ferromagnetic Ni nanostructure induces an easy-plane magnetic anisotropy, which results in rotation of the magnetization in a direction perpendicular to the strain axis. The magnetic state comprises periodic domain walls, which have a *three-dimensional* character and a spacing that depends on the dimensions of the sample. Our results demonstrate directly that strain-induced anisotropy in a nanoscale sample can lead to a modification of the magnetic state and magnetic hardening. As the strain-induced magnetic state responds differently to an external magnetic field than a strain-free state, the susceptibility also depends on strain. Similarly, charge transport is expected to depend on strain, because anisotropic magnetoresistance depends on the angle between the current and the magnetization[29]. Our unique *local* observations of tunability between strain and magnetism suggest that nanoscale ferromagnetic films can be used as sensors of directional mechanical strain, either by measuring their magnetic susceptibility or *via* transport measurements in miniature devices.

References

1. Behera, A. “Magnetostrictive materials” in *Advanced Materials.* (Springer International Publishing, 2022), pp. 140-152.

2. Novosad, V. et al. Novel magnetostrictive memory device. *J. Appl. Phys.* **87**, 6400-6402 (2000).

3. Hu, I. M., Li, Z., Chen, L. Q., & Nan, C.W. High-density magnetoresistive random access memory operating at ultralow voltage at room temperature. *Nat. Commun.* **2**, 553 (2011).

4. Roy, K., Bandyopadhyay, S., & Atulasimha, J. Hybrid spintronics and straintronics: A magnetic technology for ultra low energy computing and signal processing. *Appl. Phys. Lett.* **99**, 063108 (2011).

5. Bhatti, S., Ma, C., Liu, X., & Piramanayagam, S. N. Stress-induced domain wall motion in FeCo-based magnetic microwires for realization of energy harvesting. *Adv. Electron. Mater.* **5**, (2019).

6. Deng, Z., & Dapino, M. J. Review of magnetostrictive vibration energy harvesters. *Smart Mater. Struct.* **26**, 103001 (2017).

7. Narita, F., Fox, & M. A. Review on Piezoelectric, Magnetostrictive and magnetoelectric materials and device technologies for energy harvesting applications. *Adv. Eng. Mater.* **20**, 1700743 (2018).

8. Murzin, D. et al. Ultrasensitive magnetic field sensors for biomedical applications. *Sensors.* **20**, 1569 (2020).

9. Gao, C., Zeng, Z., Peng, S., & Shuai, C. Magnetostrictive alloys: Promising materials for biomedical applications. *Bioact. Mater.* **8**, 177-195 (2022).

10. Huber, E. E. & Smith, D. O. Properties of Permalloy Films Having a Magnetoelastic Easy Axis Normal to the Film. *J. Appl. Phys*. **30**, S91 (1959)

11. Koikeda, T., Suzuki, K. & Chikazumi, S. Electron-microscopic observation of “stripe” or “dense-banded” magnetic domains in nickel-rich permalloy films. *Appl. Phys. Lett.* **4**, 160-162, (1964)

12. Saito, N., Fujiwara, H. & Sugita, Y. A New Type of Magnetic Domain Structure in Negative Magnetostriction Ni-Fe Films. *Journal of the Physical Society of Japan* **19**, 1116-1125, (1964).

13. Zhang, J. et. al, Spontaneous Formation of Ordered Magnetic Domains by Patterning Stress, *Nano Letters*, **21**, 5430 (2021).

14. Pan, P., & Hayward, T.J. Comparative study of the giant stress impedance behavior of commercial amorphous ribbons for strain sensing applications, Journal of Applied Physics, **131**, 214503 (2022).

15. Sohn, H. et al., Electrically driven magnetic domain wall rotation in multiferroic heterostructures to manipulate suspended on-chip magnetic particles. *ACS Nano.* **9**, 4814-4826 (2015).

16. McVitie, S., McGrouther, D., McFadzean, S., MacLaren, D.A., O'Shea, K.J., Benitez, M.J., Aberration corrected Lorentz scanning transmission electron microscopy, *Ultramicroscopy* **152**, 57-62 (2015).

17. Tonomura, A. Applications of electron holography. *Rev. Mod. Phys*. **59**, 639-669 (1987).

18. Lichte, H. & Lehmann, M. Electron holography—basics and applications, *Rep. Prog. Phys*. **71**, 016102 (2008).

19. Kovács, A., Dunin-Borkowski, R. E. "Magnetic imaging of nanostructures using off-axis electron holography" in *Handbook of Magnetic Materials* (Elsevier, 2018). pp. 59-153.

20. Shibata, K. et al., Large anisotropic deformation of skyrmions in strained crystal, *Nature Nanotechnology*, **10**, 589 (2015).

21. Paterson, G. W., et al, Tensile deformations of the magnetic chiral soliton lattice probed by Lorentz transmission electron microscopy, *Physical Review B*, 101, 184424 (2020).

22. Pateras, A. et al. Room temperature giant magnetostriction in single-crystal nickel nanowires. *NPG Asia Mater.* **11**, 59, (2019).

23. Cullity, B. D., Graham, C. D. "Magnetostriction and the effects of stress" in *Introduction to Magnetic Materials*. (Wiley, 2008).

24. Wang, L. et al. Tracking the sliding of grain boundaries at the atomic scale. *Science.* **375**, 1261-1265 (2022).

25. Niitsu, K., Tanigaki, T., Harada, K., Shindo, D. Temperature dependence of 180° domain wall width in iron and nickel films analyzed using electron holography. *Appl. Phys. Lett.* **113**, (2018).

26. Soderžnik, K. Ž. et al. Microstructural insights into the coercivity enhancement of grain-boundary-diffusion-processed Tb-treated Nd-Fe-B sintered magnets beyond the core-shell formation mechanism. *J. Alloys Compd.* **864**, (2021).

27. Herzer, G., Varga, L. K. Exchange softening in nanocrystalline alloys. *J. Magn. Magn. Mater.* **215-216**, 506-512 (2000).

28. Sokolov, N. S. et al. Thin yttrium iron garnet films grown by pulsed laser deposition: Crystal structure, static, and dynamic magnetic properties. *J. Appl. Phys.* **119**, 023903 (2016).

29. McGuire, T. and Potter, R. "Anisotropic magnetoresistance in ferromagnetic 3d alloys" in *IEEE Transactions on Magnetics* (1975). **11**, pp. 1018-1038

Methods

***In situ* mechanical transmission electron microscopy.** *In situ* TEM was conducted using a home-built bimetallic deformation device from the group of Prof. Xiaodong Han in a Gatan Model 652 double-tilt heating holder in a transmission electron microscope dedicated to magnetic imaging. The bimetallic deformation device is made from two thermally-actuated bimetallic strips, which are fixed in opposing positions on a half TEM Mo ring using epoxy resin, as shown in Fig. s1a. Each bimetallic strip is made from layers of two different materials that have a large mismatch in their thermal expansion coefficients, in order to achieve a significant deflection at a relatively low operation temperature (<60 °C). The length of each strip is ~2 mm. A Si slice is fixed at the free end of each strip using epoxy resin. The distance between the two Si slices is ~30 µm. The Ni sample was prepared by using focused Ga ion beam sputtering in a dual beam scanning electron microscope (Thermo Fisher Helios 600) and positioned between the two Si slices. A T-head, hooks and an electron-transparent region were made from a Ni single crystal, as shown in Fig. s1b. In a conventional TEM heating holder, the bimetallic deformation device can be heated moderately (<60 ºC). The bimetallic strips bend in opposite directions with increasing temperature (Fig. s1c), causing the hooks to catch the T-head (Fig. s1d) and realizing an approximate uniaxial tensile test of the Ni lamella. The slightly elevated temperature (<60 °C) has only a minor impact on the magnetism of Ni, as shown in Fig. s8.

Magnetic induction mapping using off-axis electron holography. The projected in-plane magnetic induction in the Ni sample during the straining experiment was visualized and quantified using off-axis electron holography. Electron holograms were recorded using a spherical aberration corrected TEM (ThermoFisher (FEI) Titan 60-300) at 300 kV. The microscope was operated in aberration corrected Lorentz mode with the sample in magnetic-field-free conditions. Fresnel defocus images and electron holograms were recorded on a direct electron counting detector (Gatan K2 IS) with 4k resolution. The typical biprism voltage was 70 V, which corresponded to a holographic interference fringe spacing of ~4.46 nm and holographic interference fringe contrast in vacuum of ~30 %. Image analysis was performed using Gatan Microscopy Suite and HoloWorks software. Figure s2 shows the processing steps that were used to reconstruct the projected in-plane magnetic induction. Typically, electron holograms were recorded from both the Ni sample (Fig. s2a) and vacuum (Fig. s2b). The total phase shift information (Fig. s2c) was extracted using a standard Fourier transform method. The total phase shift provides information about local variations in both electrostatic and magnetic potential. Since the lamella is a single crystal and has negligible thickness variations (as shown using electron energy-loss spectroscopy (EELS) in Fig. s2e), it was assumed that the electrostatic contribution to the signal is constant and that any phase variations are magnetic in origin. Magnetic induction maps were obtained by adding contours and colors to the phase images, as shown in Fig. s2d.

180° domain wall width measurement. Figure s3 shows the procedure used for 180° domain wall width measurement. The position of a chosen 180° domain wall could be located accurately from a magnetic induction map of the lamella, as shown by a red rectangle in Fig.

s3a. The phase shift across the 180° domain wall at this position could be measured from the original phase image, as shown by a red rectangle in Fig. s3b. The width of the 180° domain wall was determined from the differential of the phase shift, as shown by a black line in Fig. s3c. Nonlinear curve fitting (red line) to the differential of the phase shift was performed using the equation

$$y = \pm a \times \tanh(\frac{\pi \times (x - x_0)}{w}) \ ,$$

where w is the width of the 180° domain wall, a is an amplitude and x_0 is an offset that can be obtained from the fit. The domain wall width obtained from this particular measurement was 53.99 ± 3.72 nm.

Micromagnetic simulations. The simulation system had dimensions of 1800x500x100 nm^3. Each cell had dimensions of 2x2x2 nm^3. The total energy density E of the Ni film with cubic symmetry was defined as

$$E = A\sum_i (\nabla m_i)^2 - M_s \boldsymbol{B} \cdot \boldsymbol{m} + K_1(\alpha_x^2\alpha_y^2 + \alpha_x^2\alpha_z^2 + \alpha_y^2\alpha_z^2) - \frac{1}{2} M_s \boldsymbol{B_d} \cdot \boldsymbol{m} + K_s(m_z)^2$$

where $A = 8.6\times10^{-12}$ J/m is the ferromagnetic exchange stiffness, m_i is the i^{th} component of the unit vector $\mathbf{m}=\mathbf{M}/M_s$ of the local magnetic moment, $M_s = 4.8\times10^5$ A/m is the saturation magnetization of Ni, $K_1 = -5000$ J/m^3 is the first order cubic anisotropy constant, α_i is the directional *cosine* with respect to the crystal axis, $\mathbf{B}$ is the external field vector, $\mathbf{B}_d$ is the local field vector due to magnetostatic dipole-dipole interactions, K_s is the strain-induced easy-plane anisotropy and m_z is a vector parallel to the strain direction.

The equilibrium magnetic state of the sample was found by numerically solving the Landau-Lifshitz-Gilbert (LLG) equation

$$\frac{\partial \boldsymbol{m}}{\partial t} = -\gamma \boldsymbol{m} \times \boldsymbol{B}_{eff} + \alpha(\boldsymbol{m} \times \frac{\partial \boldsymbol{m}}{\partial t})$$

where $\gamma=g\mu_B/\hbar$ is the gyromagnetic ratio with the Landé factor (g), the Bohr magneton (μ_B) and the reduced Planck constant ($\hbar$). The dimensionless parameter α is a measure of the Gilbert damping and the effective field in the material $\mathbf{B}_{eff} = \partial_{\mathbf{m}} E/M_s$ depends on internal and external fields. The LLG equation was integrated numerically with the software Mumax3 [30].

Figure s4 shows a summary of the micromagnetic results in the form of contour plots of the local magnetization for the Ni film under different strains. In Fig. s4(b) to Fig. s4(e), the shaded area is a guide to the eye of the narrowing of the domain wall with increasing strain-induced anisotropy; the region where the stray field closes becomes progressively smaller.

Methods references

30. Vansteenkiste, A. et al. The design and verification of MuMax3. *AIP Adv.* **4**, 107133 (2014).

Acknowledgments

The bulk Ni single crystal was kindly provided by C. Thomas and M. Feuerbacher (Forschungszentrum Jülich).

Funding

The China and Germany Postdoctoral Exchange Program 2019 from the Office of China Postdoctoral Council and the Helmholtz Centre (grant No. ZD2019020)

The European Research Council under the European Union's Horizon 2020 research and innovation programme (Grant No. 856538, project ''3D MAGiC'')

The Deutsche Forschungsgemeinschaft (DFG) through CRC270 (project-IDs 405553726, "HoMMage")

The "111" project (DB18015).

Author contributions

X.H., A.K. and R.D.B. designed the project. D.K. conducted FIB preparation and *in situ* TEM experiments. D.K., A.K. and F.Z. performed the analysis of the TEM results. M.C. performed the micromagnetic simulations. D.K., A.K., M.C. and R.D.B. wrote the manuscript. D.K., L.W. and X.H. made the bimetallic deformation device. All authors contributed to interpretation of the data and the manuscript text.

Competing interests: The authors declare no competing financial interests.

Data and materials availability: All data are available in the main text or the supplementary materials.

Supplementary Material

Figures s1-s9.
Movies s1-s3.